Fluid dynamic characterization of a fluidized-bed perfusion bioreactor with CFD-DEM simulation

Zheqing Huang[1, 2*], Akinlolu Oyekunle Oluseun Odeleye[2], Hua Ye[2], Zhanfeng Cui[2], Aidong Yang[2]

1. School of Chemical Engineering and Technology, Xi'an Jiaotong University, Xi'an, 710049, China

2. Department of Engineering Science, University of Oxford, Oxford, United Kingdom

Corresponding author: Zheqing Huang: huangzheqing@mail.xjtu.edu.cn 008617791591629

Akinlolu Odeleye: Akinlolu.odeleye@eng.ox.ac.uk 00441865617915
Hua Ye: hua.ye@eng.ox.ac.uk
Zhanfeng Cui: zhanfeng.cui@eng.ox.ac.uk
Aidong Yang: aidong.yang@eng.ox.ac.uk

Abstract:

BACKGROUND: In the recent development of regenerative medicine, the low yields of progenitor cells have shown to be among the limiting factors for large-scale clinical applications. To overcome the limitation, a novel fluidized bed perfusion bioreactor has emerged. However, a detailed understanding of the fluid dynamics of such a reactor is still lacking.

RESULTS: A three-dimensional modelling approach that couples computational fluid dynamics (CFD) and discrete element method (DEM) was used to simulate the liquid and solid flows in a bioreactor being designed for stem cells expansion. The model was validated by comparing the simulation results with literature experimental data (*Chem. Eng. Sci.* **60**: 1889-1900 (2005)), which showed a good agreement. Using the validated model, the effects of the superficial liquid velocity, particle size and particle density on the bed height, solids volume fraction, shear stress on the particles and liquid-solid mass transfer coefficient of dissolved oxygen and glucose were analyzed.

CONCLUSIONS: Simulation results show that particle size and density have an important impact on the shear stress distribution, and that the liquid velocity affects the shear stress distribution rather modestly when its value is beyond the minimum fluidization velocity. The liquid-particle mass transfer coefficient of dissolved oxygen and glucose can be improved by raising the liquid velocity, and the adoption of a high-density material allows the reactor to operate with higher liquid velocities before reaching shear stress heterogeneities. Furthermore, the two objectives, namely (i) maintaining lower and homogeneously distributed shear stress and (ii) improving mass transfer, pose conflicting requirements on certain design parameters which need to be carefully considered in the reactor design.

Keywords: liquid-solid fluidized bed, perfusion bioreactor, CFD-DEM, fluid dynamic

characterization, shear stress

NOMENCLATURE

d_p particle diameter, m

D reactor diameter, m

D_i diffusivity of species *i*, m^2/s

e_{ij} unit vector from particle *i* to *j*

f friction coefficient

F_c contact force result from the collision of the particles, N

F_d drag force between liquid and particle, N

F'_d rate of momentum exchange between the particle and liquid phase, N/m^3

F_p pressure gradient force, N

F_v virtual mass force, N

g acceleration due to gravity, m/s^2

H reactor height, m

k_{sl} solid liquid mass transfer coefficient, m/s

K spring constant, N/m

m_p particle mass, kg

M_{pj} rolling friction torque of particle p, N/m

$N_{p,c_i,t}$ particle number in cell *i* at time t

N_t number of time step (dimensionless)

$N_{\tau_k}^{\tau_{k+1}}(t)$ particle number of shear stress located between τ_k and τ_{k+1}

P liquid pressure, N/m^2

$\overline{Sh_{c_i}}$ local time averaged Sherwood number in cell *i*, dimensionless

1 $Sh_{c_i,t}$ local Sherwood number in cell *i* at time t, dimensionless

2 S_p particle surface area, m^2

3 t time, s

4 Δt fluid time steps, s

5 T_{pj} torques generated by tangential forces, N/m

6 v_{ij} relative velocity of particle *i* and *j*, m/s

7 v_l local liquid velocity, m/s

8 v_p particle velocity, m/s

9 $\overline{v_{p,z,c_i}}$ local time averaged axial particle velocity in cell *i*, m/s

10 $v_{p,z,c_i,t}$ local axial particle velocity in cell *i* at time t, m/s

11 V_l superficial liquid velocity, m/s

12 V_{mf} minimum fluidization velocity, m/s

13 V_p particle volume, m^3

14 V_{c_i} volume of cell *i*, m^3

15 Dimensionless number

16 $Re_p = \dfrac{d_p\left(v_l - v_p\right)\rho_l}{\mu_l}$ particle Reynolds number based on the relative velocity

17 $Re'_p = \dfrac{d_p V_l \rho_l}{\mu_l}$ particle Reynolds number based on superficial liquid velocity

18 $Sc = \dfrac{\mu_l}{\rho_l D_i}$ Schmidt number

19 $Sh = \dfrac{d_p k_{sl}}{D_i}$ Sherwood number

20 Greek letters

21 β interphase momentum exchange coefficient, kg/(m^3s)

γ damping coefficient

δ overlap size, m

ε_l local liquid volume fraction

$\overline{\varepsilon_{p,c_i}}$ local time averaged liquid volume fraction in cell

ρ_l liquid phase density, kg/m^3

η damping coefficient

μ_l liquid phase viscosity, kg/(ms)

τ shear stress on a particle, Pa

τ_l viscous stress tensor, kg/(ms^2)

ω_p particle rotational velocity, 1/s

Subscripts

l liquid phase

p particle phase

INTRODUCTION

The development of regenerative medicines, including cell-based therapies such as human mesenchymal stem cells (hMSCs) to treat defects in the body and tissue replacement, has been rapidly evolving during the last decade [1, 2]. However, low yields of progenitor cells due to suboptimal cell culture strategies have shown to be among the limiting factors for large-scale clinical applications [3]. To overcome the limitation, perfusion bioreactors have emerged as a valuable tool in improving cell culture processes in terms of the delivery of oxygen and nutrients and the removal of waste products [4, 5], with benefits demonstrated for various 3D cell culture purposes [3, 6, 7]. However, compared to the work on fluidized-bed reactors for other areas, studies on applications in biotechnology are still rather limited [8, 9]. Meissner *et al.* [10] compared two perfusion systems, fixed bed and fluidized bed bioreactors, with respect to their capability to support the cultivation and expansion of human hematopoietic cells. Wang *et al.* [11] showed that a Cytopilot fluidized bed bioreactor for the use of porous carriers enabled entrapped CHO cells to reach a high cell density and favorable metabolism for product release. Kinasiewicz *et al.* [12] investigated the influence of C3A cell culture in alginate beads on the synthetic function in a fluidized bed. Kong *et al.* [13] reported the comparison of CHO cell perfusion cultures in a spin-filter stirred tank bioreactor and a fluidized bed bioreactor; the results demonstrated that the CHO culture in the fluidized bed bioreactor achieved higher cell density and productivity.

In the fluidized bed perfusion bioreactor considered in this work, carrier particles are used to provide a large surface area to expand adherent stem cells for autologous cell therapy applications. The mechanism of stem cells attachment to the surface is via the cell's integrins (e.g. the triamino acid sequence, RGD). The integrin on the cells binds to this RGD group via intermolecular forces

(such as ionic bonds, hydrogen bonds and Van der Waals forces); an enzyme called trypsin can be used to break these bonds and release cells from their attached surface during the harvest [14, 15]. The bioreactor is to be operated in a semi-fluidized regime whereby the media, cells and particles are mixed by fluidization to uniformly distribute the available surface area to the cells, as shown in Figure 1.

Although fluidized beds have been widely used in many processes such as crystallization, adsorption, ion exchange, sedimentation and catalytic conversion [16-18], the development and application for 3D culture of stem cells pose a unique set of requirements, especially in terms of shear stress control and its interplay with some other aspects of the process such as mass transfer enhancement. The fluid shear force or hydrostatic pressure between the fluid and particle phases and the transport performance of controlling nutrients and waste products in a fluidized bed perfusion bioreactor will determine the cells' mechanical and chemical environment and their differentiation fate [19-22]. For example, the proliferation and differentiation of osteoblasts were enhanced in the shear stress range of 0.5-1.5 Pa using 2-D planar plates [23-27], while an average surface stress of 5×10^{-5} Pa was found to increase the cells' viability and proliferation [28-29] in 3-D constructs. Oxygen tension, on the other hand, has also shown effects on a range of cellular events, such as cell attachment and spreading [30-31], proliferation[30], migration [32] and differentiation [33-34]. These investigations suggest that an understanding and characterization of the fluid dynamic behavior and the related transport performance can play an important role in guiding the design and operation of fluidized-bed perfusion bioreactors such as the one considered in this work which is for the expansion of mesenchymal stem cells. For this specific application, the intended range of shear stress is below 1 Pa, determined based on the literature evidence that levels of shear stress

beyond this range may lead to unwanted induction of differentiation [35, 36].

In the studies of complex reactors, computer simulation has proven to be a useful tool, by providing detailed information about the local velocity field or concentration profile, especially in the regions where measurements are either impossible or difficult to obtain. In recent years, the coupled approach of computational fluid dynamics (CFD) and discrete element modeling (DEM) has been developed. This approach models the fluid phase as a continuum and tracks each particle by solving Newton's equations of motion [37]. As such, it enables the study of important details such as the fluid-particle or particle-particle interaction forces. In the applications on a liquid-solid fluidized beds, Apostolou *et al.* [38] used this approach to predict the flow of suspensions of particles in viscous liquids using DEM; the particle-particle and particle-wall colloidal, hydrodynamic and soft-sphere collision forces and the Stokes drag from the suspending medium were considered in their model. Di Renzo *et al.* [37] used a coupled CFD-DEM model to simulate the liquid-fluidization of glass beads and gas-fluidization of Geldart's Group A particles. Di Renzo *et al.* [39] and Zhou *et al.* [40] investigated the layer inversion phenomenon in liquid-fluidized beds involving a binary mixture of particles. Mukherjee et al. [41] investigated the significance of the fluid velocity in improving the separation efficiency using both DEM simulation and experimentation. Wang *et al.* [42] also applied the approach to study the flow behavior of both phases in a liquid-solid fluidized bed, with a model incorporating the lubrication force. These studies show that, for in a liquid-solid fluidized bed reactor system, CFD-DEM is an effective approach to generating detailed local dynamic information such as particle trajectories and transient forces acting either on individual particles or between the particles and the fluid.

The purpose of this study is to use numerical simulation to predict the effect of key design

parameters on the performance of a novel liquid-solid fluidized bed bioreactor currently being developed for the expansion of stem cells (and hMSC in particular). As shown in Figure 1, this apparatus is intended to host particles fluidized in the liquid culture medium that continuously passes through the reactor. It should be noted that oxygen is supplied with the liquid feed in a dissolved form, therefore the system contains liquid and solid flows, but not a gaseous phase. The particles provide the surfaces required for the hMSCs to attach and proliferate, which is affected by a number of factors, including particularly shear stress and the mass transfer of oxygen, substrates and metabolites. A three-dimensional CFD-DEM model is used in this work to provide desirable predictions. The model is first validated by comparing the simulation results with experimental data in the literature. Subsequently, the effect of the superficial liquid velocity, particle size and particle density on the liquid holdup, the shear stress on each particle, the shear stress distribution and the mass transfer coefficient of dissolved oxygen and glucose are investigated, aiming to generate an understanding of the fluid dynamics and the mass transfer potential of the bioreactor which is important for its intended application for hMSC culture.

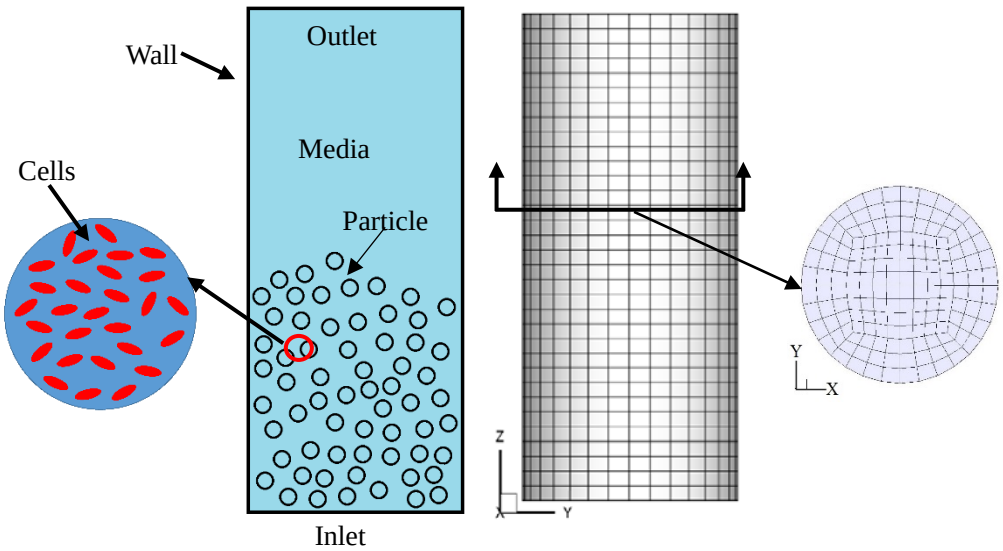

Figure 1. Physical model (left) and computational mesh (right). Cells growth was not modelled in this work.

NUMERICAL METHODS

As well-documented in the literature [43-48], the key aspect of a CFD-DEM model is the consideration of the particle-fluid, particle-particle, and particle-wall forces, such as the buoyancy force, drag force, pressure gradient force, as well as the virtual mass force and contact force. In principle, a CFD-DEM simulation tracks each particle by solving Newton's equations of the motion, while the fluid is treated as the continuum and modelled by the Navier-Stokes equations. Focusing on the interactions between the liquid phase and the carrier particles, this work does not model explicitly the stem cells attached to the carrier particles. As such, the effect of attached cells on the drag force is neglected. Besides, the mass transfer resistance modelled is between the liquid phase and the outer surface of the particles with attached cells; mass transfer within the layer of attached cells is outside the scope of the current model. Similarly, implications of the process and the uniformity of cells attachment are not considered.

Governing equations of the discrete particles

Each particle has two types of motion, translational and rotational. The linear and angular velocities of each particle, v_p and ω_p, are governed by Newton's 2nd law:

$$m_p \frac{dv_p}{dt} = F_d + F_p + F_v + m_p g + F_c \tag{1}$$

$$I_p \frac{d\omega_p}{dt} = \sum_{j=1}^{k_i} \left(T_{pj} + M_{pj} \right) \tag{2}$$

where m_p represents particle mass. F_d, F_p, F_v and F_c are four forces, namely the drag force between the liquid phase and the particle phase, the pressure gradient force, the virtual mass force and the contact force resulting from the collision of the particles, respectively. T_{pj} and M_{pj} represent the torque generated by the tangential forces, and the rolling friction torque of particle *p*, respectively. In this study, other fluid-particle forces (e.g. Basset force and lubrication force) are neglected, due to the lack of reliable correlations for such forces in dense systems and the related

difficulties in characterizing the transient fluid-particle momentum exchange [37, 39, 49].

The drag force between the liquid phase and the particle phase depends on the relative velocity between the particles and fluid, and the local solid volume fraction:

$$F_d = \frac{\beta V_p \left(v_l - v_p \right)}{1-\varepsilon_l} \tag{3}$$

where V_p, v_l, β, ε_l are the particle volume, the local liquid phase velocity, the interphase momentum exchange coefficient, and the local liquid phase volume fraction, respectively.

The drag model to estimate β is vital for quantifying solid-fluid interactions, with a significant influence on the behavior of the bed. In this study, the correlation proposed by Gibilaro *et al*. [50] was used to calculate the drag force between the two phases. The correlation, derived based on theoretical considerations, has previously been compared with experimental results and shown to represent a significant improvement over the established Ergun equation [51]. Therefore, it is considered to be able to offer a reliable prediction of the interaction between a particle and its surrounding fluid in a fluidized suspension [52-54].

$$\beta = \left(\frac{18}{Re_p} + 0.33 \right) \frac{\rho_l \left| v_l - v_p \right|}{d_p} \left(1-\varepsilon_l\right) \varepsilon_l^{-2.8} \tag{4}$$

$$Re_p = \frac{\left| v_l - v_p \right| \rho_l d_p}{\mu_l} \tag{5}$$

Re_p is the Reynolds number of the particle, ρ_l, μ_l and d_p are the liquid density, liquid viscosity and particle diameter, respectively. The virtual mass force is attributed to the particles accelerating through the fluid and a corresponding acceleration of the fluid, modeled as follows [55, 56]:

$$F_v = 0.5(1-\varepsilon_l)\rho_l \left(\frac{dv_l}{dt} - \frac{dv_p}{dt} \right) \tag{6}$$

The contact forces due to the particle-particle and particle-wall collisions were calculated according to the soft-sphere approach based on the spring dashpot collision law [57]. The force on particles *i* and *j* (F_c) was calculated as follows:

$$F_c = \left(K\delta + \gamma \left(v_{ij} e_{ij} \right) \right) e_{ij} \tag{7}$$

K is the spring constant, δ and v_{ij} are the overlap and relative velocity of particle *i* to particle *j*, respectively; and e_{ij} is unit vector from particle *i* to particle *j*.

Governing equations of the liquid phase

The fluid phase flow was modelled by a local averaged approximation of the continuity and Navier-Stokes equations with a scale of the order of the computational cell size (several particle diameters). The governing equations for the liquid-phase continuity and momentum conservation are:

$$\frac{\partial \left(\varepsilon_l \rho_l \right)}{\partial t} + \nabla \cdot \left(\varepsilon_l \rho_l v_l \right) = 0 \tag{8}$$

$$\frac{\partial \left(\varepsilon_l \rho_l v_l \right)}{\partial t} + \nabla \cdot \left(\varepsilon_l \rho_l v_l v_l \right) = -\varepsilon_l \nabla P + \varepsilon_l \rho_l g + \varepsilon_l \nabla \cdot \left(\tau_l \right) - F_d^{'} \tag{9}$$

where $F_d^{'}$ is the rate of momentum exchange between the particulate and fluid phases, τ_l is the viscous stress tensor (in Newtonian fluid) and given by:

$$\tau_l = -\frac{2}{3} \mu_l \left(\nabla \cdot v_l \right) I + \mu_l \left(\left(\nabla v_l \right) + \left(\nabla v_l \right)^T \right) \tag{10}$$

The rate of momentum exchange between the particulate and fluid phases was calculated by adding up the fluid force acting on the individual particles in a fluid cell; the force depends on not only the relative velocity between the particle and the fluid but also the presence of the neighboring particles. The drag force is expressed as follows:

$$F_d^{'} = \frac{1}{V_{cell}} \sum_{n=1}^{n=N_p} \frac{\beta V_p \left(v_l - v_p \right)}{1-\varepsilon_l} \tag{11}$$

V_{cell} is the volume of cell, N_p is the particle number in the cell.

Table 1. Parameters and Operational Conditions Adopted in the Simulation

	Case1	Case2	Case3	Case4	Case5	Case6	Case7
d_p (mm)	3	5	3	4	5	3	3
ρ_p (kg/m^3)	1100	1100	1100	1100	1100	1025	1200
ρ_l (kg/m^3)	998	998	998	998	998	998	998
μ_l (Pa·s)	0.001	0.001	0.001	0.001	0.001	0.001	0.001
f	0.3	0.3	0.3	0.3	0.3	0.3	0.3
N_p	17600	6300	17600	9900	6300	17600	17600
K (N/m)	800	800	800	800	800	800	800
u_l (cm/s)	0.2, 0.5, 1.0, 1.5, 2.0, 2.5	0.2, 0.5, 1.0, 1.5, 2.0, 2.5	0.75, 1.13, 1.50	1.15, 1.73, 2.30	1.50, 2.25, 3.00	0.23, 0.35, 0.47	1.33, 2.00, 2.66
u_l/u_{mf}	0.44, 1.10, 2.21, 3.31, 4.41, 5.52	0.22, 0.55, 1.10, 1.66, 2.21, 2.76	1.66, 2.50, 3.33	1.66, 2.50, 3.33	1.66, 2.50, 3.33	1.66, 2.50, 3.33	1.66, 2.50, 3.33
$u_{mf}{}^a$ (cm/s)	0.45	0.9	0.45	0.69	0.9	0.14	0.80
η	0.9	0.9	0.9	0.9	0.9	0.9	0.9
D (m)	0.1	0.1	0.1	0.1	0.1	0.1	0.1
H (m)	0.2	0.2	0.2	0.2	0.2	0.2	0.2

[a] The minimum fluidization velocity ($u_{mf}{}^a$) calculated according to Wen and Yu (1966) [58] at ε_f=0.425.

System dimensions, boundary conditions and numerical solution schemes

A three-dimensional liquid-solid fluidized bioreactor was simulated using ANSYS Fluent software package (ANSYS, USA). The reactor was 0.10 m in diameter and 0.2 m in height. The computational domain was created using a hexahedral mesh (cf. Figure 1b and 1c). The simulation parameters and operational conditions are listed in Table 1. The minimum fluidization velocity (u_{mf}) was calculated by the correlation (Wen and Yu [58], 1966). Three particle sizes were simulated in this work, while the total particle surface area remained the same in all the cases. Initially, the particles were regularly distributed in the reactor, the liquid phase velocity and particle velocity was set to zero. The uniform velocity distribution and the pressure outlet boundary conditions were given at the inlet and the outlet, respectively. The outlet pressure was set as atmospheric pressure, and the

system was isothermal (25 ℃). The concentrations of liquid phase at the inlet and outlet were assumed to be zero. The particle velocity at the inlet was set to zero, and the walls were with the no slip boundary conditions.

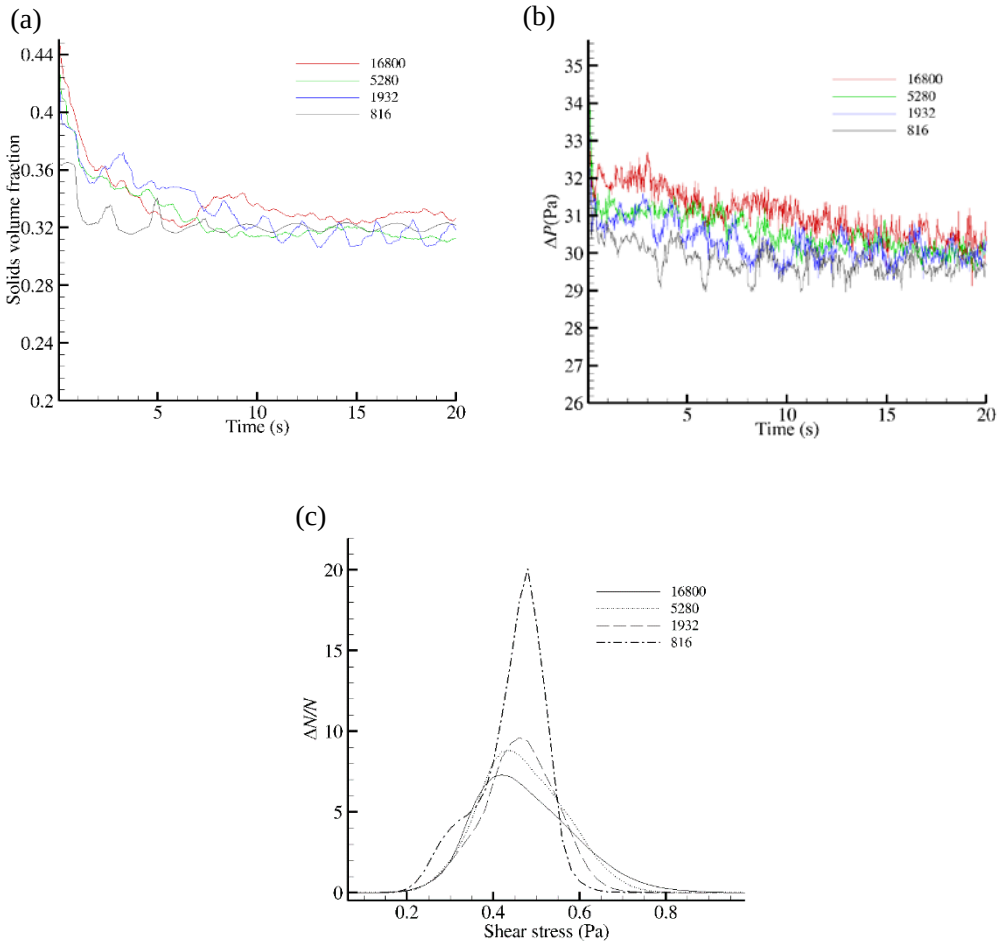

Figure 2. The effect of the mesh size on the simulation results: (a) averaged solids volume fraction vs. time; (b) pressure drop vs. time; and (c) shear stress distribution (particle size: 3 mm; density: 1100 kg/m^3; liquid velocity: 0.015m/s).

In the CFD-DEM method, the information of each particle such as velocity or position was obtained by solving the equations of particle motion. The solids volume fraction in each computational cell was calculated from the positions of the particles determined by the simulation. The differential equation to describe the liquid phase motion was solved using the SIMPLEC numerical method. The averaged velocity and pressure of the liquid phase in the fluid meshes and the solids volume fraction were used to calculate the drag force, buoyancy force, and virtual mass

force and pressure gradient force acting on the particles in the meshes. Momentum exchange between particle and fluid was calculated by averaging over the particles in a fluid mesh. At each time step, the CFD solver iterated until the flow field converged to a stable solution, and the corresponding interaction forces between liquid and particle phases were then passed to the next time step.

Determining simulation resolution

Four different mesh numbers (16800, 5280, 1932 and 816) were considered to investigate the influence of the mesh size on the simulation results; the averaged mesh sizes (in terms of the edge length of a cubic cell) were approximately equal to $1.5d_p$, $2.2d_p$, $3.1d_p$ and $4.1d_p$, respectively. The simulation results for different mesh sizes, including the averaged solids volume fraction and the pressure drop vs. time and the shear stress distribution (based on the particles from 5 s to 20 s, calculated via Eq. (12)), are shown in Figure 2. $N_{\tau_k}^{\tau_{k+1}}(t)$ is the number of particles with a shear stress located between τ_k and τ_{k+1}, N_p is the total particle number in the reactor, N_t is the number of time steps, $\frac{\Delta N_{\tau_k}^{\tau_{k+1}}}{N}$ is the percentage of particles with a shear stress falling between τ_k and τ_{k+1}. $\tau_k = \frac{F_d}{S_p}$, where F_d is the drag force between the liquid and the particle, and S_p is the particle surface area. The apparent discrepancy of shear stress distribution obtained with the mesh number of 816, compared to those from the other mesh numbers, can be seen in Figure 2c, which suggests that this lowest mesh number cannot render a realistic fluid field. It also can be seen the mesh numbers of 16800, 5280 and 1932 led to similar simulation results. Therefore, the mesh number of 5280 was adopted for all simulations in this study.

$$\frac{\Delta N_{\tau_k}^{\tau_{k+1}}}{N} = \frac{1}{N_t}\sum_{t}^{N_t}\frac{N_{\tau_k}^{\tau_{k+1}}(t)}{N_p} \tag{12}$$

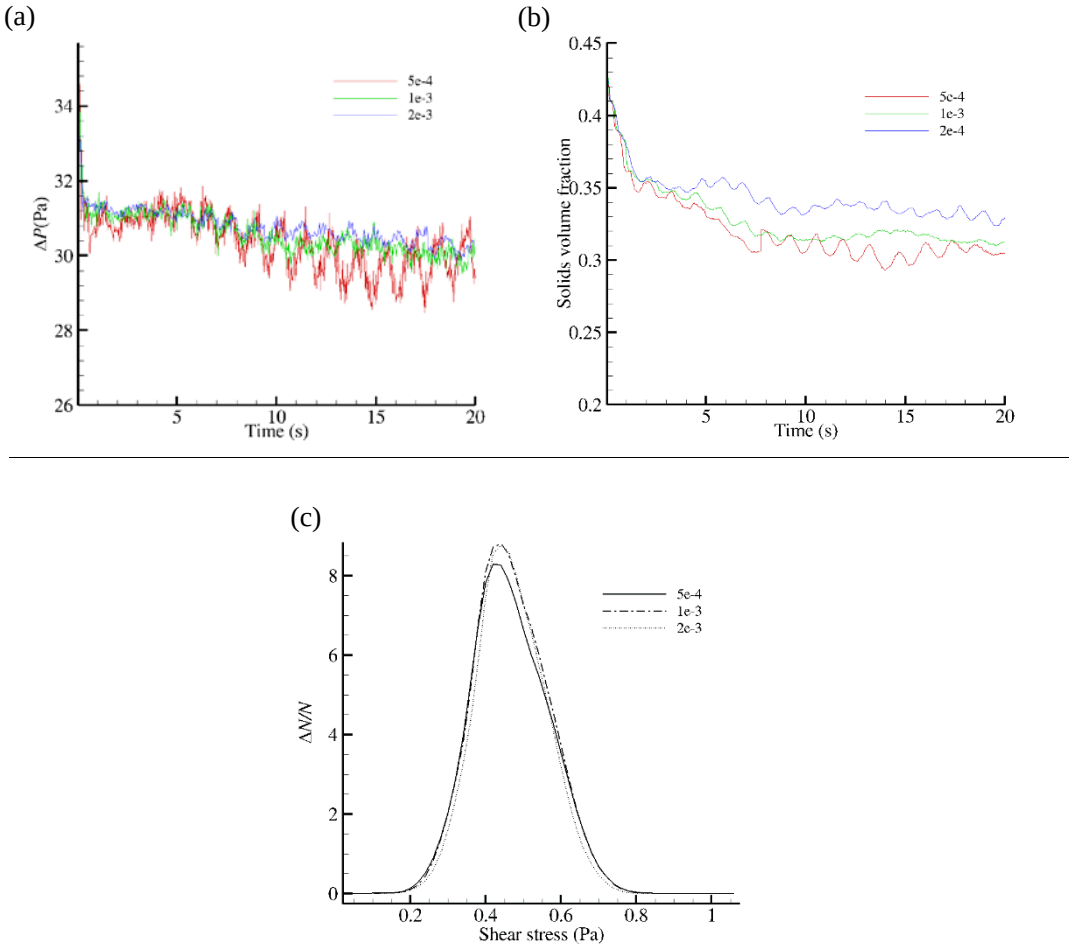

Figure 3. The effect of the time step on the simulation results: (a) averaged solids volume fraction vs. time; (b) pressure drop vs. time; and (c) shear stress distribution (particle size: 3 mm; density: 1100 kg/m^3; liquid velocity: 0.015m/s).

In CFD-DEM simulation, the time step for tracking particle was determined by $\nabla t = \pi\sqrt{m/k}/5$ [59], which is 1.9×10^{-4}s (3 mm in diameter and 1100 kg/m^3 in density) with the current computational conditions. A smaller particle time step of 1.0×10^{-4}s was used to model the contact between the particles and the collision between the particles and the bioreactor's wall. Generally, the fluid flow time step size is set to be an integer multiple of the particle time step. In this work, three fluid flow time steps 2.0×10^{-3}s, 1.0×10^{-3}s and 5.0×10^{-4}s were considered, to identify a time step size for better convergence and for accurately capturing the local hydrodynamics of the liquid-solid fluidized bed. It can be seen from Figure 3 that these time step sizes led to similar simulation results. Therefore, the time step of 1.0×10^{-3}s was used for all further simulation in this

study.

$$\overline{\varepsilon_{p,c_i}} = \frac{1}{N_t} \frac{\sum_{t}^{N_t} V_p N_{p,c_i,t}}{V_{c_i}} \tag{13}$$

$$\overline{v_{p,z,c_i}} = \frac{1}{N_t} \sum_{t}^{N_t} \frac{\sum_{k=1}^{N_{p,c_i,t}} v_{p,z,c_i,t}(k)}{N_{p,c_i,t}} \tag{14}$$

Table 2. Parameters Used in the Experiments [60] and the Present Model for Model Validation

	Experiment	Simulation
Material	Glass beads	Glass beads
d_p (mm)	3	3
ρ_p (kg/m^3)	2500	2500
ρ_l (kg/m^3)	998	998
μ_l (Pa·s)	0.001	0.001
f	-	0.3
N_p	9.7 kg	270000
K (N/m)	-	800
u_l (m/s)	0.07, 0.10,0.13	0.07, 0.10,0.13
u_l/u_{mf}	1.7, 2.4, 3.1	1.7, 2.4, 3.1
η	-	0.9
D (m)	0.14	0.14
H (m)	1.5	1.5

RESULTS AND DISCUSSION

In this section, model validation against literature experimental data is first presented. Thereafter, simulation results are presented to reveal the impact of superficial liquid velocity, particle size and particle density on solids volume fraction, shear stress, shear stress distribution and liquid-solid mass transfer. Unless specified otherwise, the simulations assume the particle size and density to be 3 mm and 1100 kg/m^3, respectively.

Model validation

The simulation results were compared with the experimental data from the work by Limtrakul

et al. [60], on a solid-liquid fluidized bed with mono-disperse glass beads. In the reported experiments, the liquid flow was measured by a turbine meter, and computer-aided radioactive particle tracking (CARPT) and computer tomography (CT) were used for the measurement of solid holdup and solid motion, respectively. Detailed settings of the experiments[57] and the simulation (this work) are listed in Table 2.

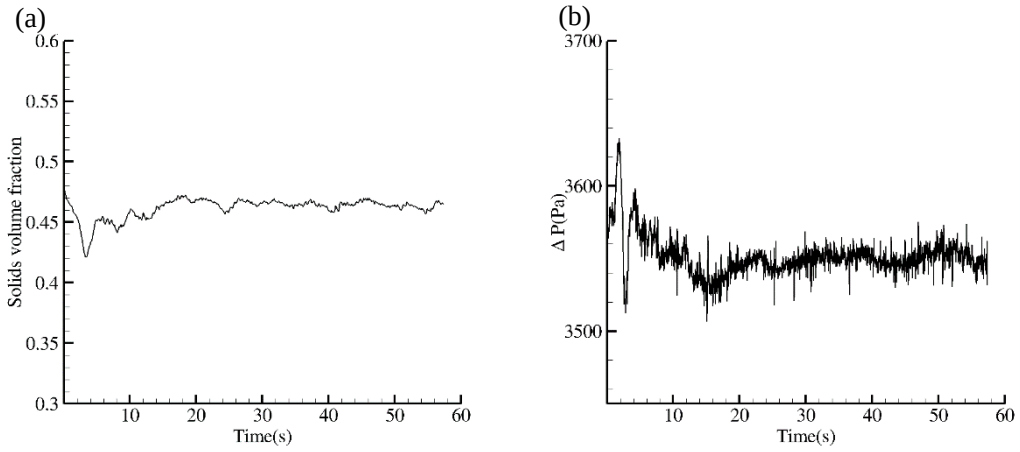

Figure 4. (a) Averaged solids volume fraction vs. time and (b) pressure drop vs. time, from CFD-DEM simulation.

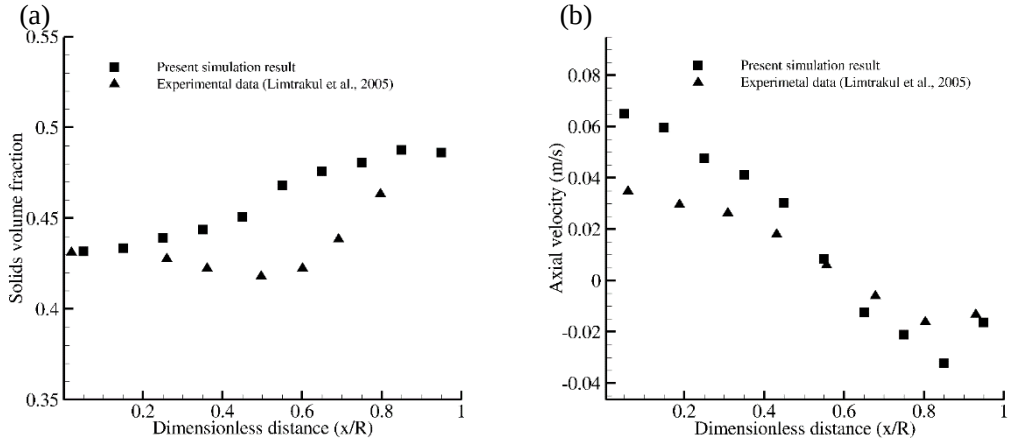

Figure 5. Comparison of simulated results and experimental measurement (Limtrakul et al. [60]) at the liquid velocity of 0.07 m/s: (a) Profile of time-averaged solids volume fraction, (b) Profile of time-averaged axial velocity.

Figure 4 shows the averaged solids volume fraction (calculated over only the cells that contain particles) and pressure drop of the bed vs. time, obtained by simulation. It can be seen that both quantities initially vary significantly but gradually settle after 10 seconds, suggesting the bed

approaches a steady state. The time-averaged overall solids volume fraction based on the data after 10 seconds was calculated as 0.46, which is very close to the experimental data (0.43) and the overall solids volume fraction of 0.44 calculated by Limtrakul et al. [60] using bed expansion and pressure drop techniques at the same operation conditions. Figure 5a compares the time-averaged radial solids volume fraction between the simulation result and the experimental data at 0.39 m above the inlet plane. The time-averaged radial solids volume fraction was calculated by the Eq. (13), where N_t is the total number of time step, V_p is the particle volume, $N_{p,c_i,t}$ is the particle number in cell *i* at time *t*, V_{c_i} is the volume of cell *i*, $\overline{\varepsilon_{p,c_i}}$ is the time averaged solids volume fraction. The simulation result shows a reasonable agreement with the experimental data, with an expected profile featuring lower values at the center and higher values near the vessel wall.

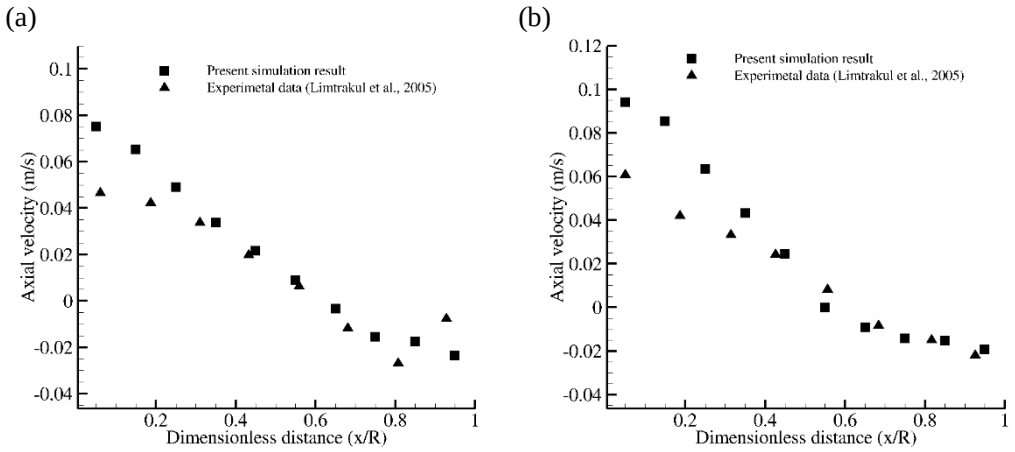

Figure 6. Comparison of time-averaged particle axial velocity between simulated results and experimental measurement (Limtrakul et al. [60]) at the different liquid velocity: (a) 0.1 m/s, (b) 0.13 m/s.

On the time-averaged axial velocity of the particles, Figure 5b shows comparable trends between the simulated result and the experimental data. The time-averaged axial velocity of the particles was calculated by the Eq. (14), where $\overline{v_{p,c_i}}$ is the time averaged axial particle velocity, $N_{c_i,t}$ is the particle number in cell *i* at time *t*, $v_{p,c_i,t}$ is the particle velocity in cell *i* at time *t*. In particular, the simulation correctly predicted that the axial velocity of particles is positive at the

center and negative near the wall; the radial transition position where a zero time-averaged axial velocity occurs appears to be between 0.55 and 0.65. This indicates that the particles flow upward at the center and downward near the wall.

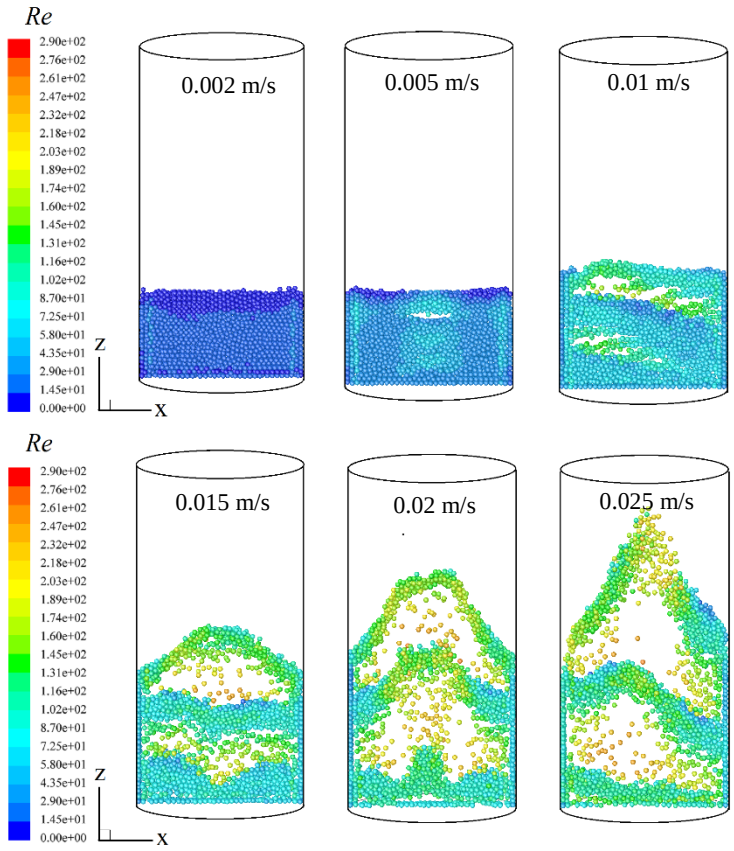

Figure 7. Profile of particle Reynolds number at different superficial liquid velocities (Case1).

Figures 6(a) and 6(b) further compare the time-averaged axial particle velocity between simulated results and experimental measurement with the liquid velocity being 0.1 m/s and 0.13 m/s, respectively, Together with Figure 5, the simulation results show a reasonable agreement with the experimental data, despite the deviation over certain intervals of the dimensionless distance which may be caused by the omission of the Basset force and the lubrication force in the model and by the empirical nature of (i) part of the model (e.g. the drag force model) and (ii) some of the model parameters (e.g. those in the collisional model). The proposed CFD-DEM model was then used to assess a liquid-solid fluidized bed bioreactor proposed for the expansion of the stem cells, with the

results presented in the following sections.

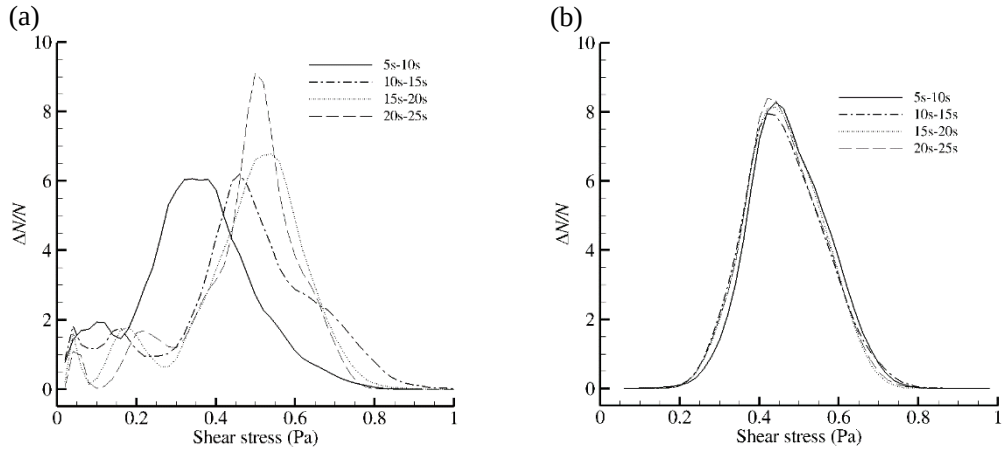

Figure 8. Distribution of shear stress on particles at two superficial liquid velocities (Case1): (a) 0.005 m/s (b) 0.015 m/s.

Effect of superficial liquid velocity

Figure 7 shows the snapshots of particles Reynolds number at 40 seconds with different liquid velocities. Only particles with their centers located in the 10 mm thick central slice of the bed in the Y direction are shown. It can be seen that the increase of liquid velocity brings a great level of energy input to the column, leading to the increase of the particles velocity, the Reynolds number and the bed height.

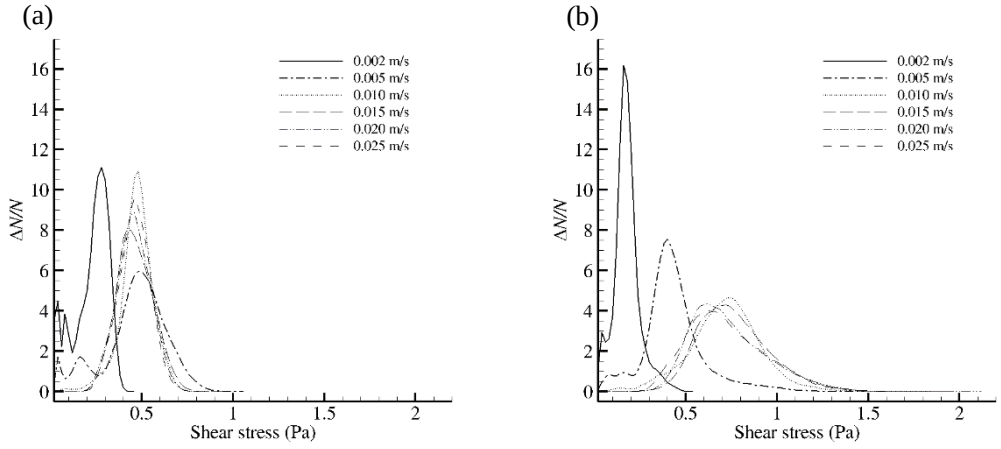

Figure 9. Distribution of shear stress on particles for different particle diameters: (a) 3 mm (Case1), (b) 5 mm (Case2).

The range of shear stress that the stem cells are exposed to can vary considerably due to the

difference in the bioreactor configuration and the operation conditions. As shear stress plays a key role in the health, proliferation and differentiation of stem cells, the shear stress distribution in the bioreactor has been analyzed at different operation conditions in this study. Figure 8 presents the distribution of shear stress on the particles averaged over each of four different time intervals with the liquid velocity spanning between 0.005 m/s and 0.015 m/s. The vertical axis is the particles number density, calculated via Eq. (12) (based on all particles in the time interval), i.e. percentage of particles falling within a unit interval of shear stress. It can be seen that the change of the shear stress after 5 seconds is very small at the liquid velocity of 0.015 m/s. The shear stress distribution also settles to a stable profile after 10 seconds at the liquid velocity of 0.005 m/s. Thus, a comparison of the shear stress distribution averaged from 10 to 20 seconds was considered for different liquid velocities, shown in Figure 9. One can see that with both particle sizes (3mm and 5mm) the liquid velocity affects the shear stress distribution rather modestly after it exceeds the minimum fluidization velocity (0.0045 m/s and 0.009 m/s, respectively). On the other hand, there is an apparent difference of the shear stress distribution between the two cases which are different in particle size, whose importance is discussed in the next subsection.

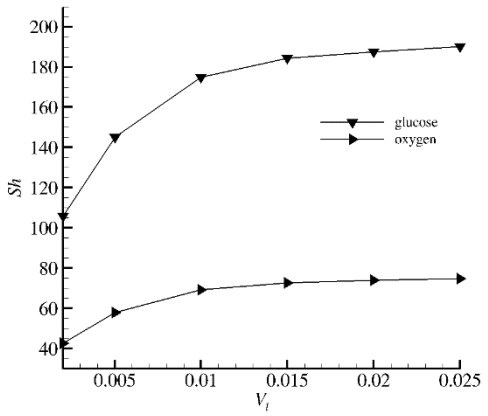

Figure 10. Overall Sherwood number of the oxygen and glucose at different liquid velocity (Case1).

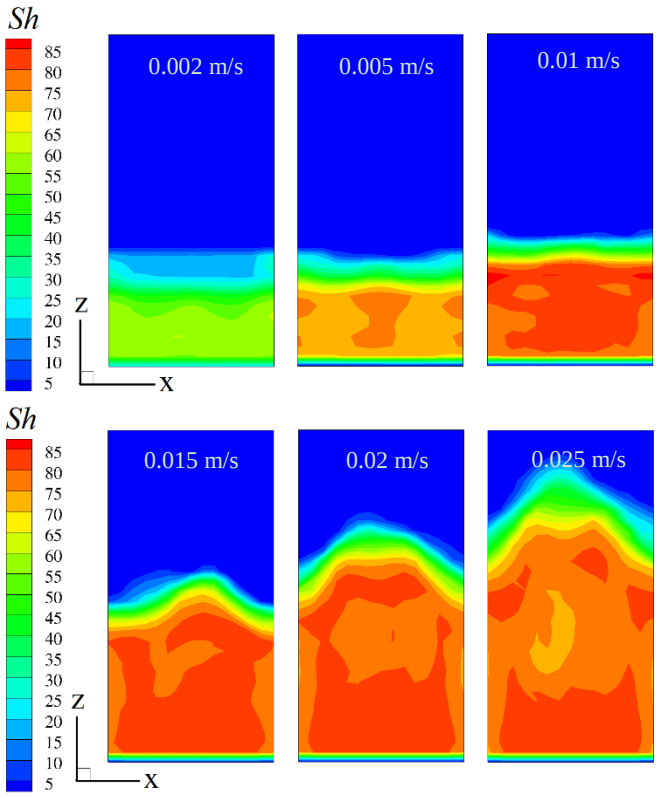

Figure 11. Time-averaged profile of *Sh* for the oxygen at different liquid velocities on the y=0 plane (Case1).

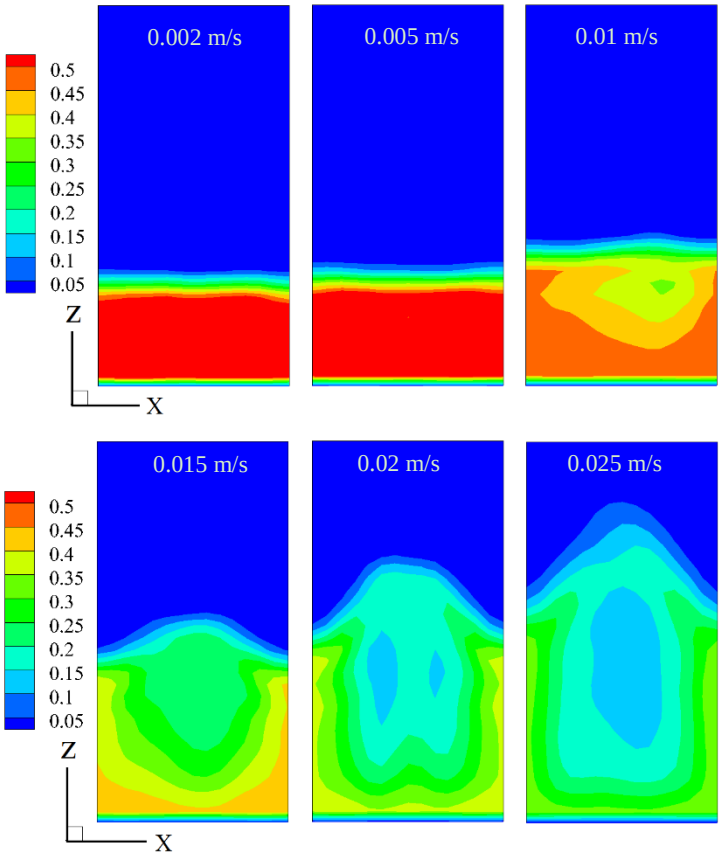

Figure 12. Time-averaged solids volume fraction at different liquid velocities on the y=0 plane (Case1).

The solid-liquid mass transfer in a fluidized bed has been widely measured in the literature, and empirical and semi-empirical correlations proposed. The well-known Froessling [61] correlation can be used to predict the mass transfer rate in a single sphere; however, for a multi-particle fluidized bed system, the mass transfer rate around one particle will be affected by the surrounded particles. In this study, the correlation proposed by Gunn [62] (Eq. (15)) was used to estimate Sherwood number (*Sh*) in the reactor, where ε_l is the voidage, $Re_p^{'}$ is the particle Reynolds number based on superficial velocity, Sc is the Schmidt number. The correlation was developed based on data obtained from experiments with fixed and fluidized beds, and has been shown to offer a reliable prediction of mass transfer in the simulation of fluid-particle systems[63, 64, 65] and provide a reasonable estimate of the Sherwood number [66].

Using Eq. (15) and the local information obtained from the CFD-DEM simulation for the fluidized bed, such as the local liquid velocity and volume fraction, and the velocity and position of each particle in all CFD-DEM cells (these parameters are assumed being homogeneous in each computational cell), local mass transfer coefficients between particles and the surrounding fluid were predicted. The diffusion coefficients for glucose (1.05×10^{-10} m^2/s) and oxygen (1.82×10^{-9} m^2/s) (needed for calculating the Schmidt number) were obtained from the literature [67, 68]. The effective diffusivity in porous media was assumed as identical to the molecular diffusivity; the porosity effects were not taken into account [69]. It can be seen from Figure 10 that the overall *Sh* of the reactor increases monotonically with an increase of superficial liquid velocity. This is due to the fact that the increase of the superficial liquid velocity intensifies the fluid flow in the vicinity of the solid-liquid interface and reduces the thickness of the liquid film around the particles, causing an increase in the mass transfer coefficient. Note that the calculation of the overall *Sh* shown in Figure

10 (and Figures 15 and 20 later in the paper) was carried out assuming homogeneous solids distribution within the reactor. In contrast, the local time-averaged *Sh* profile was calculated at the individual cells level, via Eq. (16), where $\overline{Sh_{c_i}}$ is the local time averaged Sherwood number in cell *i*, N_t is the number of time steps, and $Sh_{c_i,t}$ is local Sherwood number in cell *i* at time t. The local time-averaged *Sh* profile for the oxygen at different liquid velocities on the y=0 plane is shown in Figure 11 for a particle size of 3 mm. It can be seen that beyond the liquid velocity of 0.01 m/s, the effect of the liquid velocity on the mass transfer coefficient becomes rather insignificant. The profile for glucose (not shown) is similar. Figure 12 shows the time-averaged solids volume fraction (calculated via Eq. (13)) for different liquid velocities on the y=0 plane, indicating that the solids volume fraction (hence the number of stem cells attached to the particles surface in the bioreactor) is low in the center and high near wall, at liquid velocities greater than 0.01 m/s. Although the Sherwood number has a relatively uniform distribution in the reactor, a higher cell density in the region near the wall may lead to an insufficient supply of oxygen and glucose, particularly with liquid velocities in the upper-middle range (0.015 – 0.02 m/s), which is an aspect of the bioreactor operation that requires attention in future experimental studies.

$$Sh = (7 - 10\varepsilon_l + 5\varepsilon_l^{\,2})(1 + 0.7 Re'^{\,0.2}_{p} Sc^{0.333}) + (1.33 - 2.40\varepsilon_l + 1.20\varepsilon_l^{\,2}) Re'^{\,0.7}_{p} Sc^{0.333} \quad (15)$$

$$\overline{Sh_{c_i}} = \frac{1}{N_t} \sum_{t}^{N_t} Sh_{c_i,t} \quad (16)$$

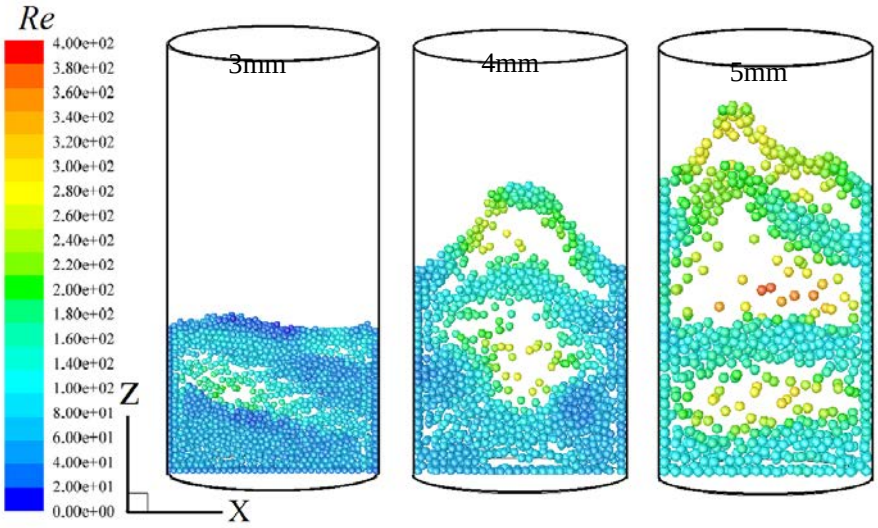

Figure 13. Profile of particle Reynolds number with different particle sizes (Case3, Case4, and Case5).

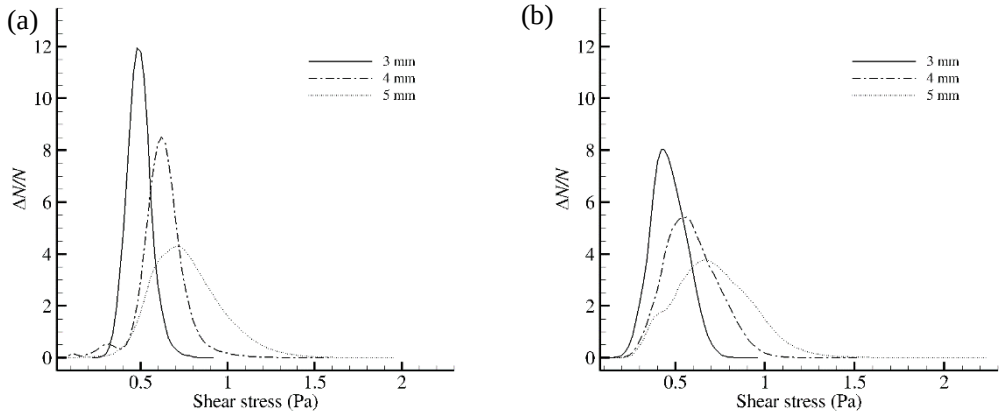

Figure 14. Distribution of shear stress on particles at two different V_l/V_{mf} (Case3, Case4, and Case5): (a) 1.66, (b) 3.30.

Effect of particle size

To investigate the effect of particle size on a comparable basis, a total particle surface area sufficient for the attachment of 5×10^8 monolayer cells was maintained across all the cases presented in this subsection, assuming a cell density of 1×10^5 cells/cm^2. Thus the particle number corresponding to a particle diameter of 3 mm, 4 mm and 5 mm are 17600, 9900 and 6300, respectively. Figure 13 shows the instantaneous particle Reynolds number and particles' position for three different particle sizes at the same operational condition V_l / V_{mf} = 2.50 (the ratio of

superficial liquid velocity to minimum fluidizing velocity). Only the particles whose centers are located in the 10 mm thick central slice of the bed in the Y direction are shown. Owing to the fact that a smaller particle size leads to a higher specific surface area, the cases with smaller particles have lower solids volume fractions when offering the same total surface area as assumed here. Therefore, the solids volume fraction monotonically increases with the increase of particle size. Figure 14 shows the time-averaged shear stress distribution based on all particles from 10 s to 20 s for three different particle sizes. It appears that the increase in particle size tends to widen the shear stress distribution and also shift the distribution towards higher values. Although not very visible from Figure 14, the simulation results showed that a small portion of the particles of 5 mm for different operational conditions reach a maximum shear stress of 2.2 Pa. Clearly, a larger particle size leads to a higher local solids volume fraction, as just discussed, which in turn results in a higher local relative velocity, hence higher shear stress. On the other hand, a larger particle size required a higher shear stress to overcome the gravity effect. These results suggest that when a larger particle size is adopted, special care needs to be given to the monitoring of the unevenness of shear stress distribution within the bioreactor and of regions of particularly high shear stress, both of which could lead to local disparity in the proliferation and differentiation of cells in the reactor. In particular, for the specific application intended by this work, i.e. expansion of MSCs, the desirable range of shear stress is below 1 Pa (as stated earlier in Introduction), the simulated distribution of shear stress for the case with 5 mm carriers suggests that this particle size might not be suitable if issues such as unwanted induction of differentiation are to be avoided.

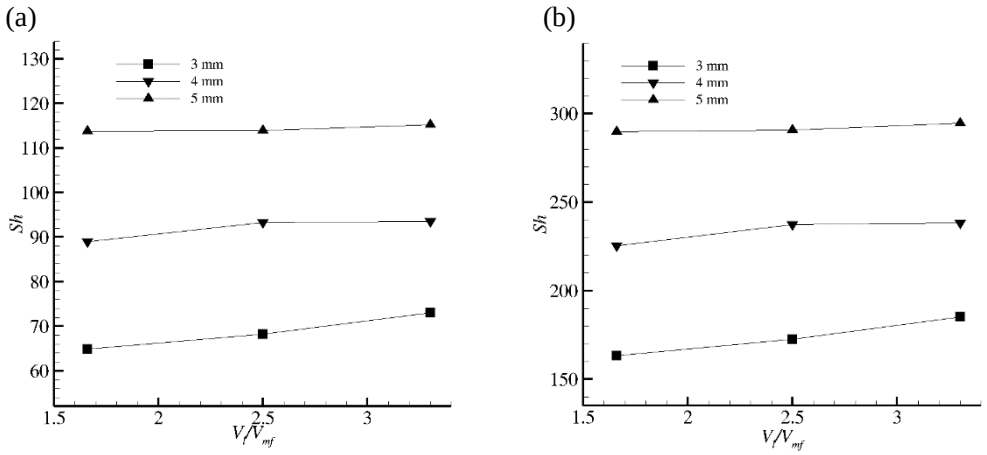

Figure 15. Overall Sherwood number of different particle size (Case3, Case4, and Case5): (a) oxygen, (b) glucose.

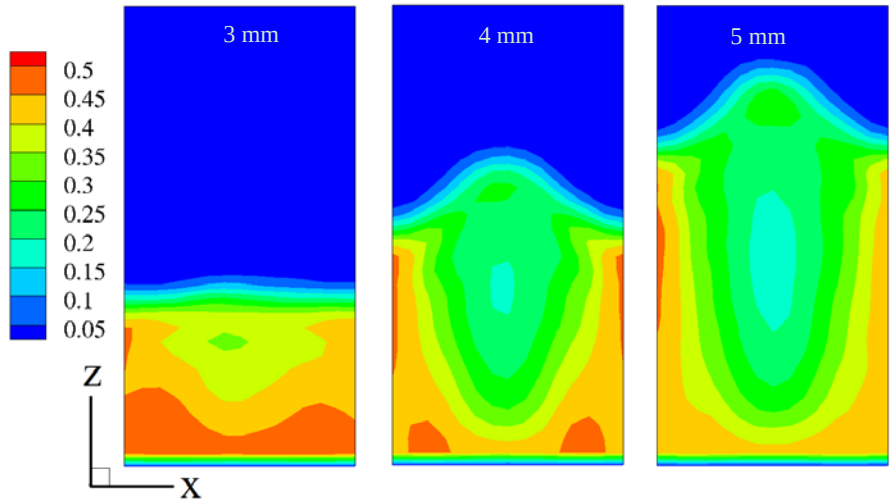

Figure 16. Time-averaged solids volume fraction for different particle sizes on the y=0 plane (Case3, Case4, and Case5).

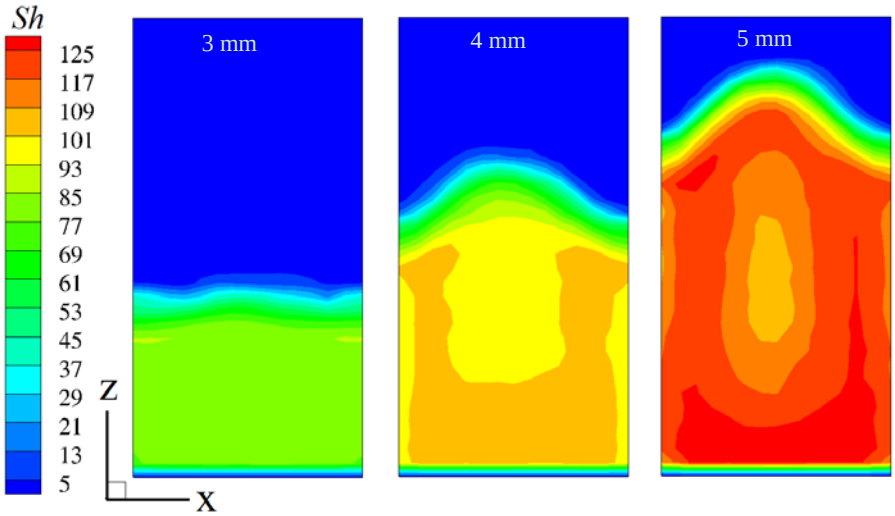

Figure 17. Time-averaged profile of Sherwood number for oxygen at different particle sizes on the y=0 plane (Case3, Case4, and Case5).

Figure 15 presents the overall *Sh* number of oxygen and glucose for different particle sizes and liquid velocities. The mass transfer coefficient increases with the particle size, which again is due to a higher local relative velocity stemming from a higher local solids volume fraction. On the time-averaged solids volume fraction, Figure 16 shows a remarkable degree of inhomogeneity within the bioreactor when V_l/V_{mf} is 2.50, observable for all particle sizes. In contrast, Figure 17 shows that a relatively uniform distribution of *Sh* is obtained regardless of the particle size. Thus, similar to what was already discussed with the effect of liquid velocity (previous section), concerns on the sufficiency of oxygen and glucose supply in these cases should be associated with high solids volume fractions at some local regions in the bioreactor, as opposed to low mass transfer coefficients.

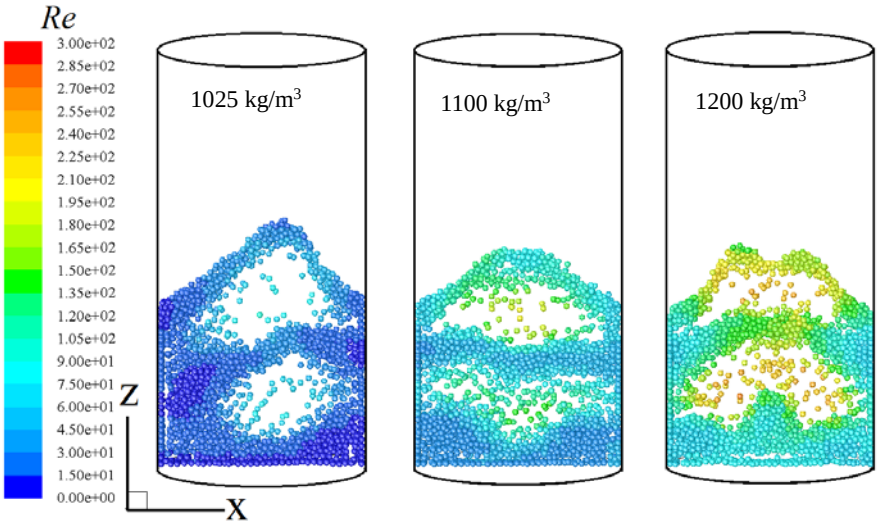

Figure 18. Profile of particle Reynolds number with different particle densities (Case3, Case6, and Case7).

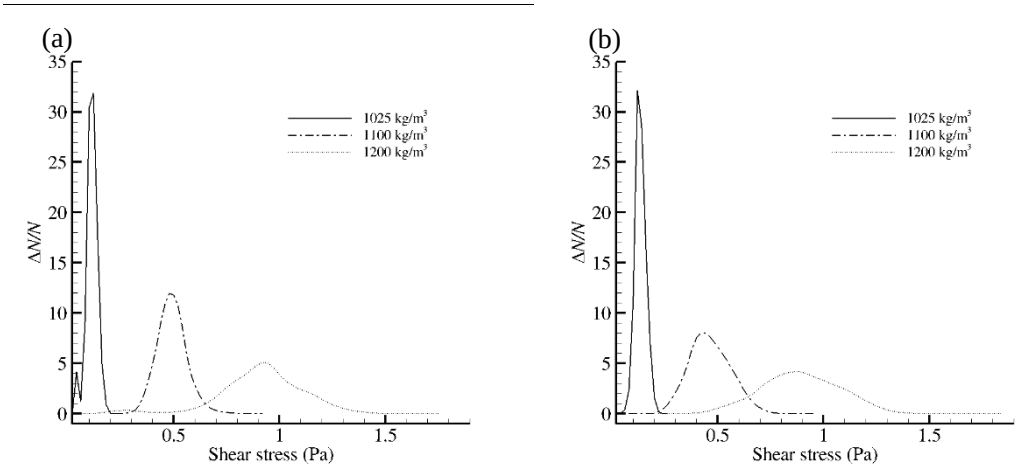

Figure 19. Distribution of shear stress on particles at two different V_i/V_{mf} (Case3, Case6, and Case7): (a) 1.66, (b) 3.30.

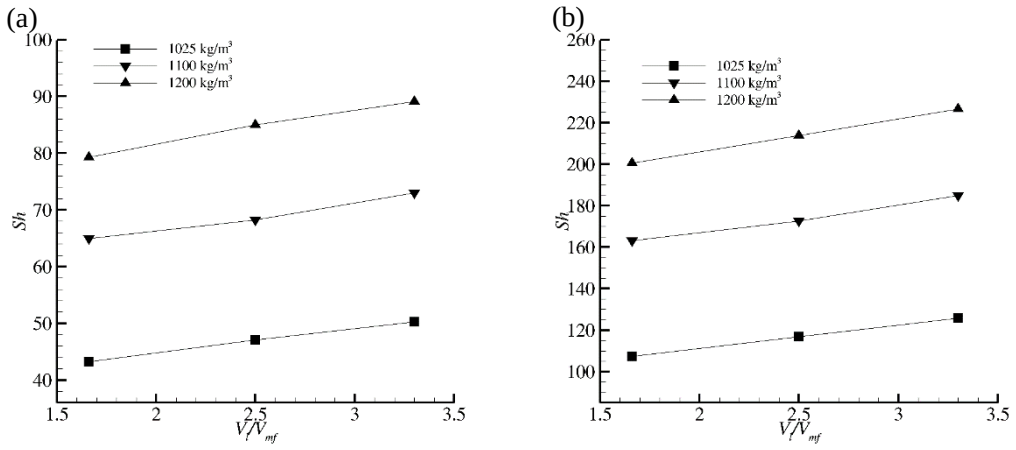

Figure 20. Overall Sherwood number of different particle density at different V_i/V_{mf} (Case3, Case6, and Case7): (a) oxygen, (b) glucose.

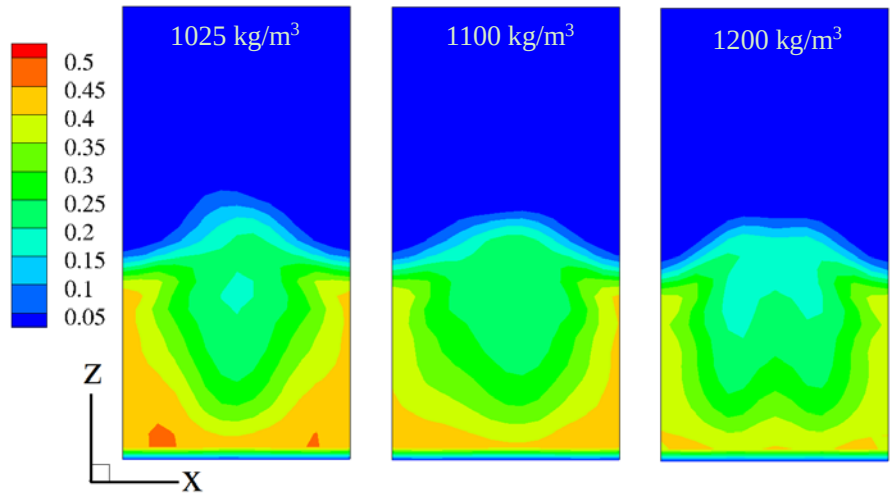

Figure 21. Time-averaged solids volume fraction for different particle densities on the y=0 plane (Case3, Case6, and Case7).

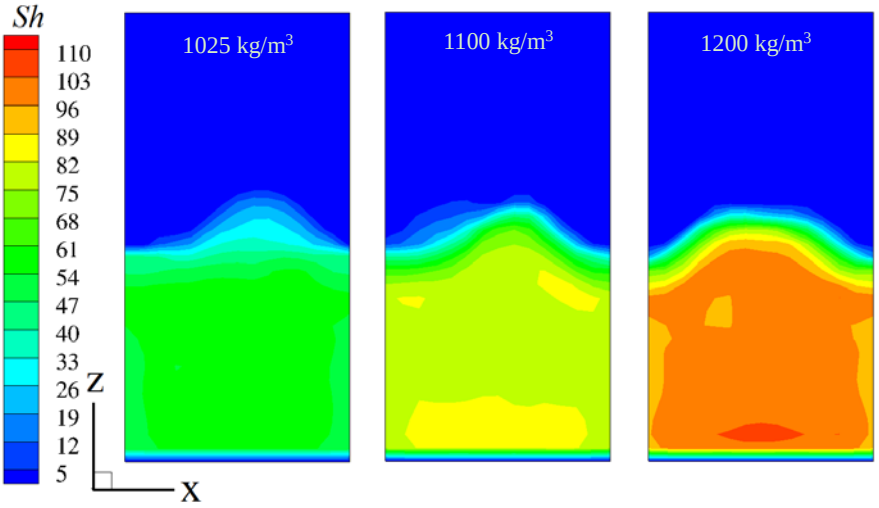

Figure 22. Time-averaged profile of Sherwood number for the oxygen on the y=0 plane (Case3, Case6, and Case7).

Effect of particle density

Figure 18 shows the instantaneous profile of particle Reynolds number (40 s) at three different particle densities when V_l / V_{mf} is 3.30. Same as before, only the particles whose centers are located in the 10 mm thick central slice of the bed in the Y direction are shown. The larger the particle density is, the higher the particle Reynolds number becomes; this is expected because the fluidized bed with a larger particles density requires a higher liquid velocity. It can also be seen that the bed expansion heights in the fluidized bed for three different particle densities at the operating condition of V_l / V_{mf} =3.30 are almost the same. Figure 19 presents the shear stress distribution based the particles from 10 s to 20 s at three different particle densities. It shows that the shear stress distribution range can increase considerably with the particle density and also shift the distribution towards higher values; the liquid velocity has little effect on the shear stress distribution. The results demonstrate that a desirable level of shear stress on particles, preferred either for cells expansion (e.g. below 1 Pa, as in the case of the application intended by this work) or for inducing the differentiation of stem cells toward specific directions (e.g. in the region of 1.5 Pa, as in some literature cases [35, 36]), can be achieved by using particles with a suitable density. On the mass transfer coefficient of the oxygen and glucose, Figure 20 shows the increase of particle density can improve the overall mass transfer rate of the oxygen and glucose in the bed. This is also expected, and is due to the fact that the particles with a larger density require a higher liquid velocity at the same operating condition (V_l / V_{mf}). With respect to the solids volume fraction, as mentioned above, Figure 21 shows similarity in the time-averaged solid volume fractions for three different particle densities, and it can be seen that the solids volume fraction is low in the core region and high near

the wall. Finally, Figure 22 shows that compared to lower particle densities, the particle density of 1200 kg/m^3 obtains a higher *Sh* due to the reason that a higher liquid velocity is required for the particle with a larger density. Overall, the simulation results indicate that particles with a density of 1025 kg/m^3 would require a lower liquid fluidization velocity and render a narrower shear stress distribution, while a low mass transfer coefficient for the oxygen and glucose is inevitable due to the low liquid velocity.

CONCLUSIONS

Considering a solid-liquid fluidized bed bioreactor proposed for the expansion of mesenchymal stem cells, this work has adopted a CFD-DEM numerical method to simulate the complex multiphase flow in the reactor and to study the impact of key process parameters. This method makes it possible to analyze the shear stress on each particle, and to generate local particle and fluid phase information in the bioreactor.

For the model validation, the time-averaged solids volume fraction and axial particle velocity predicted by the CFD-DEM model were compared with literature experimental data, which showed a good agreement. Using the validated model, effects of different operational conditions and parameters, such as the superficial liquid velocity, particle size and particle density on the bed height, solids volume fraction, shear stress on the particles and the liquid-solid mass transfer coefficient of oxygen and glucose were analyzed. Simulation results show that a specific level of shear stress on particles, as may be needed to either avoid or induce the differentiation of the stem cells, can be achieved by choosing the particles with suitable size and density; the mass transfer coefficient of oxygen and glucose can be improved by raising the superficial liquid velocity and using particles with different sizes; the liquid velocity has little effect on shear stress; and the particle density has

a great effect on the mass transfer coefficients. To improve the homogeneity of shear stress within the bioreactor as required by its intended use for hMSC culture, a smaller particle size and a lower particle density are recommended based on the observations from this study, although one should bear in mind that adopting a lower particle density may limit mass transfer due to a lower maximum liquid velocity permitted to retain the particles. This work also shows the potential of the CFD-DEM method in studying fluidized bed based 3D cell culture processes; combining this modelling technique with experimental explorations could prove fruitful in the future development of bioreactors for novel bioengineering applications.

ACKNOWLEDGEMENTS

The authors wish to acknowledge financial support by the National Natural Science Foundation of China (project No. 21406157), the China Scholarship Council (No. 201606285053), and support from China Regenerative Medicine International (CRMI).

REFERENCES

1. Hewitt CJ, Lee K, Nienow AW, Thomas RJ, Smith M and Thomas CR, Expansion of human mesenchymal stem cells on microcarriers. *Biotechnol. Let.* **33**: 2325 (2011).

2. Martin I, Baldomero H, Bocelli-Tyndall C, Passweg J, Saris D and Tyndall A, The survey on cellular and engineered tissue therapies in Europe in 2010. *Tissue Engineering Part A* **18**: 2268-2279 (2012).

3. Zhao F and Ma T, Perfusion bioreactor system for human mesenchymal stem cell tissue engineering: dynamic cell seeding and construct development. *Biotechnol. Bioeng.* **91**: 482-493

(2005).

4. Petrenko YA, Petrenko AY, Martin I and Wendt D, Perfusion bioreactor-based cryopreservation of 3D human mesenchymal stromal cell tissue grafts. *Cryobiology* **76**: 150-153 (2017).

5. Eghbali H, Nava MM, Mohebbi-Kalhori D and Raimondi MT, Hollow fiber bioreactor technology for tissue engineering applications. *The International journal of artificial organs* **39(1)**: 1-15 (2016).

6. Fröhlich M, Grayson WL, Marolt D, Gimble JM, Kregar-Velikonja N and Vunjak-Novakovic G, Bone grafts engineered from human adipose-derived stem cells in perfusion bioreactor culture. *Tissue Engineering Part A* **16(1)**: 179-189 (2009).

7. Wendt D, Marsano A, Jakob M, Heberer M and Martin I, Oscillating perfusion of cell suspensions through three‐dimensional scaffolds enhances cell seeding efficiency and uniformity. *Biotechnol. Bioeng.* **84(2)**: 205-214 (2003).

8. Godia F and Solà C, Fluidized-bed bioreactors. *Biotechnol. Progr.* **11**: 479-497 (1995).

9. Schügerl K, Three-phase-biofluidization—application of three-phase fluidization in the biotechnology—a review. *Chem. Eng. Sci.* **52**: 3661-3668 (1997).

10. Meissner P, Schröder B, Herfurth C and Biselli M, Development of a fixed bed bioreactor for the expansion of human hematopoietic progenitor cells. *Cytotechnology*, **30(1)**, 227-234 (1999).

11. Wang MD, Yang M, Huzel N and Butler M, Erythropoietin production from CHO cells grown by continuous culture in a fluidized‐bed bioreactor. *Biotechnol. Bioeng*, **77(2)**, 194-203 (2002).

12. Kinasiewicz A, Gautier A, Lewinska D, Bukowski J, Legallais C and Weryński A, Culture of C3A cells in alginate beads for fluidized bed bioartificial liver. In *Transplantation proceedings*, *Elsevier*, **39(9)**, 2911-2913 (2007).

13. Kong D, Cardak S, Chen M, Gentz R and Zhang J, High cell density and productivity culture of Chinese hamster ovary cells in a fluidized bed bioreactor. *Cytotechnology*, **29(3)**, 215-220 (1999).

14. Sawyer AA, Hennessy KM and Bellis SL, The effect of adsorbed serum proteins, RGD and proteoglycan-binding peptides on the adhesion of mesenchymal stem cells to hydroxyapatite. *Biomaterials* **28(3)**, 383-392 (2007).

15. Sawyer AA, Hennessy KM and Bellis SL, Regulation of mesenchymal stem cell attachment and spreading on hydroxyapatite by RGD peptides and adsorbed serum proteins. *Biomaterials* **26(13)**, 1467-1475 (2005).

16. Roy S and Dudukovic MP, Flow mapping and modeling of liquid− solid risers. *Ind. Eng. Chem. Res.* **40**: 5440-5454 (2001).

17. De Felice R, Hydrodynamics of liquid fluidization. *Chem. Eng. Sci.* **50**: 1213–1245 (1995).

18. Epstein N, Applications of liquid–solid fluidization. *Int. J. Chem. React. Eng.* **1** (2003).

19. Zhao F, Chella R and Ma T, Effects of shear stress on 3 - D human mesenchymal stem cell construct development in a perfusion bioreactor system: Experiments and hydrodynamic modeling. *Biotechnol. Bioeng.* **96**: 584-595 (2007).

20. Stolberg S and McCloskey KE, Can shear stress direct stem cell fate?. *Biotechnol. Progr.* **25**: 10-19 (2009).

21. Jeong JY, Park SH, Shin JW, Kang YG, Han KH and Shin JW, Effects of intermittent hydrostatic pressure magnitude on the chondrogenesis of MSCs without biochemical agents under 3D co-culture. *J. Mater. Sci. Mater. M.* **23**: 2773-2781 (2012).

22. Wang YK and Chen CS, Cell adhesion and mechanical stimulation in the regulation of mesenchymal stem cell differentiation. *J Cell. Mol. Med.* **17**: 823-832 (2013).

23. Jiang GL, White CR, Stevens HY and Frangos JA, Temporal gradients in shear stimulate osteoblastic proliferation via ERK 1/2 and retinoblastoma protein. *Am. J. Physiol-Endoc M.* **283**: E383-E389 (2002).

24. Klein-Nulend J, Helfrich MH, Sterck JGH, MacPherson H, Joldersma M, Ralston SH and Burger EH, Nitric oxide response to shear stress by human bone cell cultures is endothelial nitric oxide synthase dependent. *Biochem. Bioph. Res. Co.* **250**: 108-114 (1998).

25. Mc Allister TN, Du T and Frangos JA, Fluid shear stress stimulates prostaglandin and nitric oxide release in bone marrow-derived preosteoclast-like cells. *Biochem. Bioph. Res. Co.* **270**: 643-648 (1998).

26. Reich KM and Frangos, JA, Effect of flow on prostaglandin E2 and inositol trisphosphate levels in osteoblasts. *Am. J. Physiol -Cell Ph.* **261**: 428-432 (1991).

27. Smalt R, Mitchell FT, Howard RL and Chambers TJ, Induction of NO and prostaglandin E2 in osteoblasts by wall-shear stress but not mechanical strain. *Am. J. Physiol-Endoc M.* **273**: 751-758 (1997).

28. Cartmell SH, Porter BD, García AJ and Guldberg RE, Effects of medium perfusion rate on cell-seeded three-dimensional bone constructs in vitro. *Tissue Eng.* **9**: 1197-1203 (2003).

29. Porter B, Zauel R, Stockman H, Guldberg R and Fyhrie D, 3-D computational modeling of media flow through scaffolds in a perfusion bioreactor. *J Biomech.* **38**: 543-549 (2005).

30. Mitchell SA, Poulsson AHC, Davidson MR, Emmison N, Shard AG and Bradley RH, Cellular attachment and spatial control of cells using micro-patterned ultra-violet/ozone treatment in serum enriched media. *Biomaterials* **25**: 4079-4086 (2004).

31. Rotem A, Toner M, Bhatia S, Foy BD, Tompkins RG and Yarmush ML, Oxygen is a factor

determining in vitro tissue assembly: Effects on attachment and spreading of hepatocytes. *Biotechnol. Bioeng.* **43**: 654-660 (1994).

32. Annab B, Lee YT, Turcotte S, Naud E, Desrosiers RR, Champagne M and Beliveau R, Hypoxia promotes murine bone‐marrow‐derived stromal cell migration and tube formation. *Stem cells* **21**: 337-347 (2003).

33. Cipolleschi MG, Sbarba PD and Olivotto M, The role of hypoxia in the maintenance of hematopoietic stem cells. *Blood* **82**: 2031-2037 (1993).

34. Terai H, Hannouche D, Ochoa E, Yamano Y and Vacanti JP, In vitro engineering of bone using a rotational oxygen-permeable bioreactor system. *Mater. Sci. Eng. C* **20**: 3-8 (2002).

35. Wang H, Riha GM, Yan S, Li M, Chai H, Yang H and Chen C, Shear stress induces endothelial differentiation from a murine embryonic mesenchymal progenitor cell line. *Arteriosclerosis, thrombosis, and vascular biology* **25(9)**: 1817-1823 (2005).

36. Kobayashi N, Yasu T, Ueba H, Sata M, Hashimoto S, Kuroki M, and Kawakami M, Mechanical stress promotes the expression of smooth muscle-like properties in marrow stromal cells. *Experimental hematology* **32(12)**: 1238-1245 (2004).

37. Di Renzo A and Di Maio FP, Homogeneous and bubbling fluidization regimes in DEM–CFD simulations: hydrodynamic stability of gas and liquid fluidized beds. *Chem. Eng. Sci.* **62**: 116-130 (2007).

38. Apostolou K and Hrymak AN, Discrete element simulation of liquid-particle flows. *Comput. Chem. Eng*. **32**: 841-856 (2008).

39. Di Renzo A, Cello F and Di Maio FP, Simulation of the layer inversion phenomenon in binary liquid--fluidized beds by DEM–CFD with a drag law for polydisperse systems. *Chem. Eng. Sci.* **66**:

2945-2958 (2011).

40. Zhou ZY and Yu AB, Simulation of the flow and segregation of particle mixtures in liquid fluidization. In M. Nakagawa, S. Luding. *AIP Conference Proceedings* **1145**: 993-996 (2009).

41. Mukherjee AK and Mishra BK, Experimental and simulation studies on the role of fluid velocity during particle separation in a liquid–solid fluidized bed. *Int. J Miner Process.* **82**: 211-221 (2007).

42. Wang S, Guo S, Gao J, Lan X, Dong Q and Li X, Simulation of flow behavior of liquid and particles in a liquid–solid fluidized bed. *Powder Technol.* **224**: 365-373 (2012).

43. Xu BH and Yu AB, Numerical simulation of the gas-solid flow in a fluidized bed by combining discrete particle method with computational fluid dynamics. *Chem. Eng. Sci.* **52**: 2785-2809 (1997).

44. Zhu HP, Zhou ZY, Yang RY and Yu AB, Discrete particle simulation of particulate systems: theoretical developments. *Chem. Eng. Sci.* **62**: 3378-3396 (2007).

45. Tsuji Y, Tanaka T and Ishida T, Lagrangian numerical simulation of plug flow of cohesionless particles in a horizontal pipe. *Powder Technol.* **71**: 239–250 (**1992**).

46. Zhou ZY, Kuang SB, Chu KW and Yu AB, Assessments of CFD–DEM models in particle–fluid flow modelling. *J. Fluid Mech.* **661**: 482-510 (2010).

47. Deen NG, Annaland MVS, Van der Hoef MA and Kuipers JAM, Review of discrete particle modeling of fluidized beds. *Chem. Eng. Sci.* **62**: 28-44 (2007).

48. Chu KW and Yu AB, Numerical simulation of complex particle–fluid flows. *Powder Technol.* **179**: 104-114 (2008).

49. Ten Cate A and Sundaresan S, Analysis of unsteady forces in ordered arrays of monodisperse spheres. *J. Fluid Mech.* **552**: 257-287 (2006).

50. Gibilaro LG, Di Felice R and Waldram SP, Generalized Friction Factor and Drag Coefficient Correlations for Fluid-particle Interactions. *Chem. Eng. Sci.* **40**: 1817-1823 (1985).

51. Ergun S, Fluid flow through packed columns. *Chem. Eng. Prog.* **48**: 89-94 (1952).

52. Visuri O, Wierink GA and Alopaeus V, Investigation of drag models in CFD modeling and comparison to experiments of liquid–solid fluidized systems. *Int. J. Miner. Process.***104**, 58-70 (2012).

53. Das Sharma S, Pugsley T and Delatour R, Three-dimensional CFD model of the deaeration rate of FCC particles. *AIChE J.* **52(7)**, 2391-2400 (2006).

54. Lindborg H, Lysberg M, & Jakobsen HA, Practical validation of the two-fluid model applied to dense gas-solid flows in fluidized beds. *Chem. Eng. Sci.* **62(21)**, 5854-5869 (2007).

55. Crowe CT, Sommerfeld M and Tsuji Y, Multiphase flows with droplets and particles, CRC Press (1997).

56. Ishii M and Mishima K, Two-fluid model and hydrodynamic constitutive relations. *Nucl. Eng. Des.* **82**: 107–126 (1984).

57. Cundall PA and Strack ODL, A discrete numerical model for granular assemblies. *Geotechnique* **29**: 47–65 (1979).

58. Wen CY and Yu YH, A generalized method for predicting the minimum fluidization velocity. *AIChE J* **12**: 610–612 (1966).

59. Tsuji Y, Kawaguchi T and Tanaka T, Discrete particle simulation of two-dimensional fluidized bed. *Powder Technol.* **77**: 79-87 (1993).

60. Limtrakul S, Chen J and Ramachandran PA, Solids motion and holdup profiles in liquid fluidized beds. *Chem. Eng. Sci.* **60**: 1889-1900 (2005).

61. Froessling N, The evaporation of falling drops. *Gerl. Beitr. Geophys*. **52**: 170–216 (1938).

62. Gunn, DJ, Transfer of heat or mass to particles in fixed and fluidised beds. *Int. J. Heat Mass Transfer* **21(4)**, 467-476 (1978).

63. DEEN Niels G and KUIPERS JAM, Direct numerical simulation of fluid flow and mass transfer in dense fluid–particle systems. *Ind. Eng. Chem. Res.* **52(33)**: 11266-11274 (2013).

64. DERKSEN JJ, Simulations of solid–liquid mass transfer in fixed and fluidized beds. *Chem. Eng. J.* **255:** 233-244 (2014).

65. CARLOS VARAS, Álvaro E, PETERS Elias AJF and KUIPERS JAM, Computational Fluid Dynamics–Discrete Element Method (CFD-DEM) Study of Mass-Transfer Mechanisms in Riser Flow. *Ind. Eng. Chem. Res.* **56(19)**: 5558-5572 (2017).

66. Breault RW and Guenther CP, Mass transfer in the core-annular and fast fluidization flow regimes of a CFB. *Powder Technology*, **190(3)**, 385-389 (2009).

67. Casciari JJ, Sotirchos SV and Sutherland RM, Glucose diffusivity in multicellular tumor spheroids. *Cancer Res.* **48**, 3905-3909 (1988).

68. Mueller-Klieser WF and Sutherland RM, Oxygen consumption and oxygen diffusion properties of multicellular spheroids from two different cell lines. In Oxygen Transport to Tissue—VI, Springer US, 311-321 (1984).

69. Zehner P and Schlunder EU, On the effective heat conductivity in packed beds with flowing fluid at medium and high temperatures. *Chem. Ing. Tech* **42**, 933-941 (1970).